CORA Cork Open Research Archive
Cartlann Taighde Oscailte Chorcaí

Title	Structure and Dynamics of Co and Ru Adatoms and Nanoclusters on Tungsten Dichalcogenide Monolayers
Authors	Sweetman, Michael;Nolan, Michael;Nies, Cara-Lena
Publication date	2026-08-05
Original Citation	Sweetman, M, Nolan, M & Nies, C-L 2026, 'Structure and Dynamics of Co and Ru Adatoms and Nanoclusters on Tungsten Dichalcogenide Monolayers', Journal of Physical Chemistry C, vol. 130, no. 33, pp. 11738-11753. < https://pubs.acs.org/jpccck/article/doi/10.1021/acs.jpcc.6c01928/5245979/Structure-and-Dynamics-of-Co-and-Ru-Adatoms-and >
Type of publication	Article (peer-reviewed)
Link to publisher's version	https://www.scopus.com/pages/publications/105047853165, https://pubs.acs.org/jpccck/article/doi/10.1021/acs.jpcc.6c01928/5245979/Structure-and-Dynamics-of-Co-and-Ru-Adatoms-and
Rights	Publisher Copyright: © 2026 The Authors. Published by American Chemical Society - https://creativecommons.org/licenses/by/4.0/
Download date	2026-10-31 11:01:59
Item downloaded from	https://hdl.handle.net/10468/19121

UCC
University College Cork, Ireland
Coláiste na hOllscoile Corcaigh

Structure and Dynamics of Co and Ru Adatoms and Nanoclusters on Tungsten Dichalcogenide Monolayers

Michael Sweetman[1], Michael Nolan[1], and Cara-Lena Nies[1,*]

[1]Tyndall National Institute, University College Cork, Lee Maltings, Dyke Parade, Cork, T12 R5CP, Ireland

[*]Corresponding author: caralena.nies@tyndall.ie

Abstract

Tungsten dichalcogenide monolayers have unique properties which make them promising as channel materials in next-generation semiconductor devices, atomically thin diffusion barriers in interconnects, and low-dimensional supports for catalysis. These applications require interfacing the monolayer with a metal, whose morphology typically determines which applications are viable. An atomistic understanding of how metals interact and grow on these monolayers is therefore essential. Theoretical work has largely addressed single-atom adsorption and doping, or pristine metal–monolayer interfaces, leaving the early stages of metal growth unexplored. Using density functional theory, we study the relaxations and dynamics of Co and Ru adatoms, dimers, and 4-atom nanoclusters on WS_2, WSe_2, and WTe_2. This allows us to develop a comprehensive understanding of the fundamental interactions between adsorbed metal atoms and monolayers, revealing the role different metal-substrate and metal-metal interactions have in affecting preferred adsorption sites and nanocluster structure and potential morphology. We find both metals interact strongly with all three monolayers and may also induce structural changes that affect thin-film growth. The larger lattice parameters of WSe_2 and WTe_2 drive a strong preference for interstitial adsorption. Interstitial adsorption can cause displacement of W atoms in WTe_2 and trigger a local hexagonal-to-orthorhombic phase change in the monolayer. Co and Ru can also promote formation of chalcogen vacancies by displacing the chalcogen atom and occupying the resulting vacant site. Overall, Ru favours vertical growth, with stability driven by metal–metal interaction, whereas Co is most stable at interstitial sites.

1 Introduction

2D materials are a class of crystalline solids composed of a single monolayer, offering unique properties compared to their bulk counterparts which opens up novel applications in a wide range of diverse fields[1]. Transition metal dichalcogenides (TMDs) are one group of 2D materials for which the monolayers have distinct properties from the bulk, allowing for numerous applications due to their unique optical[2–5], electrical[6,7], and mechanical properties[8–10].

Bulk TMDs are layered materials which consist of covalently bonded monolayers, held together by van der Waals interactions between the layers. TMD monolayers have an X-M-X "sandwich" crystal structure where X and M are the chalcogen and metal atom respectively[11]. The properties exhibited by TMD monolayers can differ dramatically depending on both the metal, chalcogen, and crystal phase that is present[12].

Tungsten TMDs (WS_2, WSe_2, WTe_2; henceforth collectively denoted as WX_2) are important for a variety of applications such as catalysis[13–15], optoelectronics[16,17], spintronics[18,19], gas sensors[20–22], and antibacterial activity[23,24].

Metal deposition onto the substrate is central to many of these technologies, particularly for electronics and energy conversion. Understanding the early stages of metal adsorption and growth on TMD monolayers is therefore essential for the next generation of technologies in which metals are deposited on and interfaced with 2D materials. More generally, the morphology of the deposited metal is crucial in determining the possible application of a given metal-substrate combination[25]. Metals which form 3D clusters are useful in catalysis, as the high surface-to-volume ratio provides a large number of active sites[26]. In particular, TMDs have shown promise for the hydrogen evolution reaction. Although the basal plane of these monolayers is largely inert, by decorating the monolayer with a metal catalyst, a clear enhancement in activity can be delivered[27].

Conversely, metals which have a morphology characterised by lateral growth when deposited can be used as interconnects or metal contacts for semiconductor devices[28]. As transistor size decreases in accordance with Moore's law, downscaling the lowest level interconnect structures has become a bottleneck[29,30]. Cu is widely used as the interconnect metal. However at these smaller scales, the resistivity of copper increases making its use no longer viable for next-generation semiconductor devices[31–34]. In addition, the diffusion barrier layer, typically TaN with an additional liner of Ru or Ta to promote Cu plating, consumes a significant fraction of the available volume. As a result, TMDs have been suggested as atomically thin diffusion barriers, which would increase the available volume for the interconnect metal in the via and therefore keep line resistance low[35–38]. For this to be viable, the interconnect metal must wet the diffusion barrier to form a smooth, conductive film. However, previous work has shown that Cu does not wet TMD monolayers[39,40] at very low film thickness. Therefore, further combinations of TMD diffusion barriers and interconnect metals for downscaled complementary metal-oxide semiconductor (CMOS) technology nodes needs to be explored, to enable next generation technology such as Gate-All-Around and Complementary Field Effect Transistors.

The elemental metals Co and Ru show promise to replace Cu as the line-level metal in interconnect structures due to their lower resistivity at nanometre-scale dimensions[41–45]. Understanding the preferred growth mode of these metals on candidate barrier layers is therefore crucial in determining which TMD-interconnect combination is suitable for next-generation semiconductors.

Current literature investigating the interaction of Co and Ru with 2D TMD monolayers typically involves the adsorption of or doping with single metal atoms in order to investigate the effect on magnetic and electronic[46–49], optical[50], and gas sensing properties[51–53]. However, investigation beyond single metal atoms on WX_2 to understand the initial stages of metal growth and predict thin-film morphology is lacking.

To address this, we provide an atomistic description of Co and Ru adsorption and dynamics on three tungsten TMD monolayers with different chalcogen species (WS_2, WSe_2, and WTe_2), with clusters of 1, 2, and 4 metal atoms. From this we extract metal-metal and metal-surface interaction energies. Using the relative magnitude of and competition between these energies we infer the likely early-stage growth mode on each monolayer. Our previous work on Cu adsorption onto TaN[54–56], MoS_2[39], WX_2[40], and Co and Ru on MoS_2[57] has shown that if metal-metal interactions are stronger than metal-surface interactions, a vertical growth mode of the metal is preferred. However, if metal-substrate energies dominate, lateral growth is preferred, suggesting the metals will form the targeted continuous thin films[54,55].

We perform 0 K structural relaxations, *ab initio* molecular dynamics (aiMD), and nudged elastic band (NEB) calculations to probe stability and dynamics of adsorbed metals on these monolayers. It should be noted that for WTe_2 the most stable phases are 1T and 1T', with the 2H phase being metastable[58–60]. Despite this, the 2H

phase has been fabricated and characterised[61], and is not merely a model consideration, but a real material of interest. We investigate WTe_2 in the metastable 2H phase as it is a semiconducting phase with unique properties, making it particularly interesting for use as a channel material in tunnel field-effect transistors[62]. In contrast, the 1T and 1T' phases are not semiconducting and are therefore unsuitable for use as a channel material[63]. Furthermore, by examining three WX_2 monolayers with the same hexagonal crystal structure, we determine the effect of the chalcogen species and lattice parameter on the stability of metal adsorption and on final metal morphology.

2 Computational Methods

All calculations were performed with density functional theory (DFT) using the Vienna Ab initio Simulation Package (VASP) version 5.4.4[64]. Periodic three-dimensional boundary conditions were applied, and the spin-polarized general gradient approximation (GGA) using the Perdew–Burke–Ernzerhof (PBE) approximation to the exchange–correlation functional were used[65].

The core electrons were described using the projector-augmented wave potential (PAW)[66,67]. The valence electrons were described explicitly using a plane-wave basis set with an energy cut-off of 450 eV. The valence electron configurations used for the chemical species for all relaxations and nudged elastic band calculations are: W = $6s^1$ $5d^5$; S = $3s^2$ $3p^4$; Se = $4s^2$ $4p^4$; Te = $5s^2$ $5p^4$; Co = $3d^8$ $4s^1$; Ru = $4d^7$ $5s^1$. A Monkhorst–Pack k-point grid of 2×2×1 was used. All forces acting on the atoms were converged to within 0.02 eV/Å, with convergence criteria for energy minimisation set to 10^{-4} eV for geometry relaxations. A Methfessel–Paxton smearing of order 1 was used and no symmetry was applied. We use a smearing of $\sigma = 0.1$ eV to treat partial occupancies.

For *ab initio* molecular dynamics (aiMD) simulations, a plane wave energy cut-off of 250 eV and Gaussian smearing with $\sigma = 0.1$ eV were used. Simulations were performed in the canonical (NVT) ensemble using a Nosé-Hoover thermostat with a heat bath at 500 K, and a timestep of 5 fs for a total simulation time of 15 ps. The final structures of the geometry optimisations were used as the starting structure of the aiMD simulations. The lower energy cut-off facilitates configurational exploration and longer time-scales given limited computing resources. We note that at this lower energy cut-off, the forces are already well converged and the energies are off-set by a constant, compared to 450 eV. Any new configurations obtained from these aiMD runs were relaxed at 0 K with an energy cut-off of 450 eV, to compute accurate energy differences. For a detailed description of convergence tests and error analysis, see Supporting Information.

Activation energies were calculated using the climbing image nudged elastic band method with 5 intermediate images. An energy cut-off of 450 eV was used with forces on intermediate images converged to 0.05 eV/Å[68,69]. Activation energies for reactions are calculated using $E_{Act} = E^{\ddagger} - E_{IS}$, where E_{Act} is the activation energy, E_{IS} is the energy of the starting geometry and $E_{\ddagger}$ is the energy of the transition state between starting geometry and final geometry. Activation energy for the reverse process is calculated in the same way, but with respect to the energy of the final geometry, rather than the starting geometry.

From our previous work[39,40,57] we use a 5×5×1 supercell of WX_2 monolayers, where X is either S, Se, or Te, with 75 monolayer atoms in the supercell and a vacuum region greater than 17 Å along the z-direction to prevent interaction of periodic images. These WX_2 monolayers have the same 2H hexagonal structure as MoS_2 monolayers, only differing by lattice parameter and the metal-chalcogenide bond length. While 2H WTe_2 is metastable, it has been successfully synthesised[61].

Van der Waals corrections were not used as we have previously shown that van der Waals interactions do not contribute significantly to the stability and optimised geometry of metal clusters on TMD monolayers[57]. Structures were visualised using the atomic simulation environment (ASE) and VESTA[70,71]. Atomic charges were computed from the Bader charge partitioning scheme[72,73].

To understand the adsorption of Co and Ru atoms and predict the likely growth mechanism of these metals on each WX_2 monolayer, we compute four different types of energy according to our previously published workflow for predicting the morphology of metal thin-films deposited on various substrates[40,54–57].

1. The binding energy per metal atom:

$$E_{bind/atom} = \frac{E_{total} - (E_{monolayer} + nE_{\mathrm{metal-atom}})}{n} \quad (1)$$

where E_{total} is the total energy of the relaxed cluster-monolayer system. We refer to the metal cluster itself as M_n (M = Co/Ru, $n = 1, 2, 4$). $E_{monolayer}$ is the energy of the bare monolayer, and $nE_{metal-atom}$ is the energy of a single gas phase metal atom multiplied

by n, the number of metal atoms adsorbed on the surface.

2. The interaction energy between adsorbed metal atoms, referred to as the metal-metal interaction energy:

$$E_{metal-metal} = \frac{E_{metal-cluster} - nE_{metal-atom}}{n} \quad (2)$$

Where $E_{metal-cluster}$ is the single point energy of the relaxed, surface bound M_n nanocluster structure in vacuum, with n being the number of metal atoms in this cluster.

3. The binding energy with reference to free metal cluster ($E_{metal-cluster}$, see Eq. 2), also referred to as the metal-substrate interaction energy:

$$E_{metal-substrate} = \frac{E_{total} - (E_{monolayer^*} + E_{metal-cluster})}{n} \quad (3)$$

Here $E_{monolayer^*}$ is the single point energy of the monolayer with no metal, in the relaxed structure it obtains during metal adsorption. We use this energy, rather than the monolayer energy used in equation 1, as the adsorption of metal atoms can introduce a local strain and distortion to the monolayer. This adsorption induced strain has an associated energy cost, which means the total energy of the monolayer may be significantly altered from that of the bare monolayer.

From these equations it is possible to disaggregate the overall binding energy per atom into its components, namely metal-surface interactions, metal-metal interaction, and a surface distortion term.

$$E_{bind/atom} = E_{metal-surface} + E_{metal-metal} + E_{distortion} \quad (4)$$

where

$$E_{distortion} = \frac{E_{monolayer^*} - E_{monolayer}}{n} \quad (5)$$

We also compare these results for Co and Ru to our previous work on the adsorption of Cu onto MoS_2[39] and WX_2[40], and Co and Ru onto MoS_2[57], to broadly contextualise our results in reference to trends occurring across different adatom species and transition metal dichalcogenide monolayers.

We calculate the energy required for formation of chalcogen vacancies based on the reaction H_2 + MX_2 $\rightarrow MX_2(V_X)$ + H_2X where M is the metal species (Mo, W) and X is the chalcogen (S, Se, Te). The chalcogen vacancy formation energy is then found using

$$E_{vac} = E_{H_2X} - \left((E_{MX_2} - E_{MX_2(V_X)}) + E_{H_2}\right) \quad (6)$$

3 Results and Discussions

To investigate the early stages of metal nucleation on these TMD monolayers, M_n (M = Co/Ru, $n = 1, 2, 4$) nanoclusters are adsorbed onto the TMD monolayers at different sites in different initial configurations. Binding energies for each structure are calculated using equation 1, metal-substrate interaction energies are calculated using equation 3, and metal-metal interaction energies are calculated using equation 2. These energies are displayed for every structure in Tables S1, S2, S4, S5 and S6 of the Supporting Information.

For Co and Ru on WX_2 there are five unique adsorption sites in contrast to our previous work involving Cu adsorption onto WX_2[40], in which only four stable sites were found. The five adsorption sites are as follows: **Atop-X**, where the adatom adsorbs directly above a chalcogen; **Atop-M** where the metal adatom adsorbs above tungsten so that it is coordinated to three chalcogen atoms; **Hollow**, where the adatom is coordinated to three chalcogen atoms but where there is no tungsten atom underneath the adsorbed species; **Bridge**, where the atom is at a bridging site between two chalcogen atoms and **Interstitial**, where the metal adatom has situated below the **hollow** site to be in the tungsten plane of the monolayer rather than on the surface, which was not seen for copper on WX_2.

These sites with the exception of **Bridge** are shown in figure 1. Adsorption at **Bridge** site is shown in figure S2 in the Supporting Information as it is generally not stable upon relaxation, and only exists for a few configurations. For the sake of brevity, an atom's initial adsorption site will be referred to as **X**, **M**, **H**, **I**, or **B** for **Atop-X**, **Atop-M**, **Hollow**, **Bridge** and **Interstitial** respectively.

From the large number of geometries investigated (>250 initial structures), we discuss only those directly relevant to metal adsorbate stability in the main manuscript, particularly as different starting structures can relax to the same final geometry. A complete set of figures for all optimised geometries is provided in the Supporting Information (SI, Figures S1 - S15).

Regarding the morphology of the adsorbed metal, we distinguish between 2D and 3D structures. A structure is considered 2D if all metal atoms are bound to the

WX_2 monolayer (X being S, Se, or Te). In a 3D structure however, at least one metal atom is not bound to the monolayer, but only to other metal adatoms (*e.g.* four atom tetrahedron with the apex atom only bound to the base metal adatoms).

3.1 Single atom adsorption

Adsorption at site **X**, **M**, **H**, and **I** is exothermic for both Co and Ru atoms on all three monolayers. A stable adsorption structure at site **B** was only found for Co on WS_2. For all other site **B** relaxations, the metal adatom migrated into either the adjacent **M** or **H** site. This is in contrast to the adsorption of Cu onto WX_2, where adsorption at site **B** is stable on all three monolayers. Adsorption energies for all sites with the exception of site **B** on WS_2 are shown in table 1 and figure 3, with the metal-TMD distances shown in figure 4.

Table 1: Single-atom adsorption energies.

	Site	WS_2 (eV/atom)	WSe_2 (eV/atom)	WTe_2 (eV/atom)
Co	X	−1.12	−0.87	−0.87
	M	−2.61	−2.21	−2.36
	H	−1.34	−1.23	−1.42
	I	−2.18	−2.10	−4.12
Ru	X	−1.52	−1.19	−1.32
	M	−2.85	−2.53	−2.88
	H	−1.81	−1.59	−2.08
	I	−2.01	−2.61	−4.52

The binding energy for Co at site **B** is −1.27 eV. This site was not stable for any other structure.

For both metal species, adsorption onto the telluride monolayer is the most stable adsorption mode, followed by the sulphide, and then the selenide. The stability of an adsorption site is not correlated with the bond length between the adsorbed metal and the atoms in the monolayer. Rather, adsorption stability is determined by the coordination environment and thus the site at which the atom adsorbs. This behaviour was seen in our previous work on metal-TMD adsorption[39,40,57], where the distance of the adsorbed metal to the TMD was not related to the overall binding energy.

The range of binding energies over the adsorption sites is largest on the telluride monolayer, due to the significant stability of adatom adsorption at site **I**, which is by far the most stable site on all monolayers. Figure 2 displays the most stable single atom adsorption modes for both metals on each monolayer. For both Ru and Co, adsorption at site **I** on WTe_2, Fig. 2c) and f), is ~ 3.2 eV stronger than the least stable site, **X**, which is the least stable adsorption mode for both metal atoms on all three monolayers. For WS_2 and WSe_2 however, this difference in stability between the most and least stable site is only ~ 1.4 eV. This arises from the fact that the lattice constant of WTe_2 is larger than that of the sulphide and selenide, allowing both Ru and Co species to be situated at site **I** in the plane of the tungsten atoms without a large distortion of the monolayer, while WSe_2 must distort from its equilibrium structure to accommodate the interstitial metal atom. This is also seen from the different interaction energies: Ru has a metal-substrate interaction energy of ~ -7.1 eV for adsorption at site **I** on both WSe_2 and WTe_2. However, the distortion energy on WSe_2 is 4.52 eV, 1.90 eV larger than it is for WTe_2 (2.62 eV), thereby significantly reducing the overall binding energy, Eq. 4.

Unlike the telluride and selenide monolayers, WS_2 does not allow incorporation of the adsorbed metal adatoms into the **I** site in the tungsten layer of the TMD. Rather, atoms adsorbed at site **I** on WS_2 sit in the same layer as the chalcogen atoms. This results in a reduced activation barrier when compared to the selenide and telluride migration between sites **H** and **I**. Due to this, adsorption at site **M**, rather than site **I**, is the most stable adsorption site for both metal atoms on WS_2. For Cu, Co, and Ru adsorption onto MoS_2 and Cu adsorption on WX_2, site **M** was also the most favourable single atom adsorption site. This trend likely holds across the different transition metal disulphides as MoS_2 and WS_2 have similar lattice constants of 3.16 and 3.18 Å respectively. Therefore, the geometric environment which drives single atom adsorption is similar for all adsorbed metal species on MoS_2 and WS_2.

By comparing the adsorption of Co and Ru at sites **M** and **I** on WS_2, the role of adatom size on adsorption stability becomes clear. Adsorption of Co at site **M** is 0.43 eV more stable than at site **I** on WS_2. For Ru however, this difference is notably larger, with adsorption at site **M** being 0.84 eV more stable than at site **I** on WS_2. Ru has an atomic radius of 1.78 Å, 0.26 Å larger than Co[74,75]. This means the volume a Ru atom occupies is about 1.7 times larger than for a Co atom. Therefore, Ru cannot bind as favourably to site **I** as Co can, reducing the Ru binding energy at site **I** on WS_2.

On WSe_2, adsorption at sites **I** and **M** is much more competitive. For Co, site **M** is the most stable mode on WSe_2, whereas for Ru, site **I** is the most stable site. The difference in stability however, is only about 0.1 eV

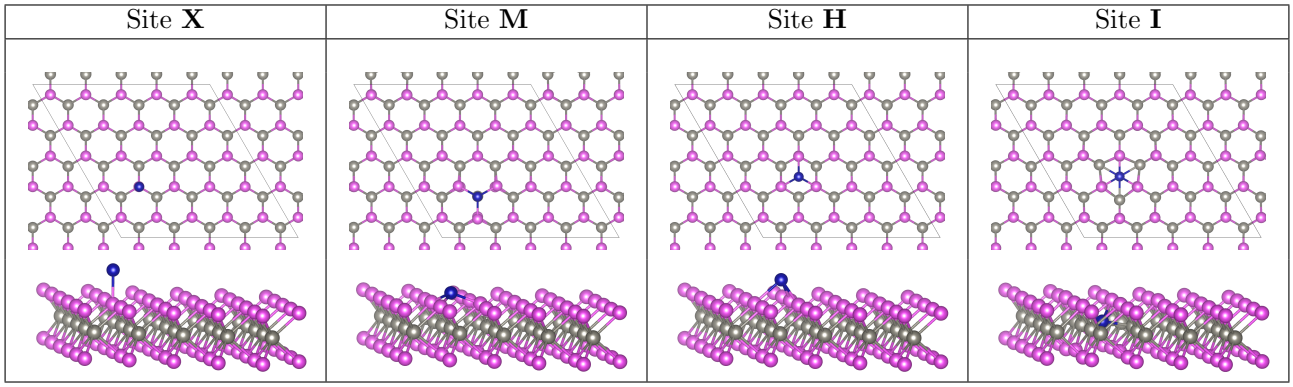


Figure 1: Adsorption structures of a single Co atom on WX_2 to illustrate the four main adsorption sites. The example used is a single cobalt atom on WTe_2. Site **B** can be seen in Figure S2 of the Supporting Information. Atomic colours are as follows: grey = W; purple = Te; blue = Co.

for both metal atoms. This is unlike the behaviour seen on WS_2 or WTe_2, where a clear preference is shown for binding at either site **M** or **I** respectively.

The Ru adsorption geometry at site **I** on WSe_2 is different from other site **I** adsorption modes, figure 2 (e). Here, the Ru atom relaxes to the edge of the **interstitial** site, rather than the centre. This geometry has a very large metal-surface energy of −7.13 eV, while also having a very large distortion energy of 4.52 eV, showing that stable adsorption geometries of metal atoms can be found, even with large distortions to the monolayer, which is balanced by the strong metal-WX_2 interaction. This was also observed for the adsorption of Co and Ru onto MoS_2[57], where stable structures were found that heavily distorted the monolayer. The large distortions on MoS_2 are compensated by strong metal-substrate interaction, leading to an overall favourable adsorption configuration. On the contrary Cu was not found to distort MoS_2 or WX_2 significantly.

To explore the dynamics of possible transitions between adsorption sites at finite temperature, aiMD was performed at 500 K on all relaxed **metal** and **hollow** site adsorption structures for 15 ps. This temperature is typical of back-end-of-the-line processing temperatures and while 15 ps is relatively short, it is sufficiently long to provide useful information regarding the dynamics of metal adatoms on TMD substrates and explore the configurational space of metals on these monolayers in a computationally tractable manner. These sites are chosen as they allow us to investigate the possible migration of an adatom across the surface of the monolayer, as well as providing insight into the transition from either site **M** or **H** to site **I**. The final frame of these simulations was then relaxed, with relevant structures shown in figure 2. The path of atoms which migrated over the course of aiMD is also shown in figure 5.

For aiMD adatoms initially at site **M**, no migration of Co or Ru occurs on WS_2, or for Co on WSe_2. This is due to the adsorption site **M** being the most stable single atom adsorption mode for these metal-WX_2 combinations. For the remaining three structures, namely Ru on WSe_2, and Co and Ru on WTe_2, the metal atoms migrate to their most stable site found during 0 K relaxation.

Ru adsorbed at site **M** on WSe_2 remains at this site for $\sim$ 7 ps, after which it migrates to the edge of site **I**. On WTe_2, both Co and Ru migrate to site **I** after $\sim$ 3.5 ps. The migration of the Ru atom to site **I** causes a displacement of tungsten atoms in the monolayer on WTe_2, resulting in formation of a locally orthorhombic structure.

On all three monolayers, Co atoms initially at site **H** migrate to site **I** and remain at this site for the remainder of the simulation; these transitions occur in less than 1 ps. Geometry relaxation of the final frame of each aiMD simulation confirms that all Co structures show the same binding energy as the original relaxations, demonstrating that at typical CMOS fabrication temperatures transitions between site **H** and **I** may occur spontaneously. We find the activation barrier for this transition is 0.003, 0.12, and 0.08 eV respectively, with the reverse transition being 0.84, 0.98, and 2.78 eV respectively. Figure 3 shows the relative stabilities of adsorption sites and the activation barriers for selected migrations between sites.

For Ru initially at site **H** on both WS_2 and WSe_2, rather than Ru migration to site **I**, the chalcogen mi-

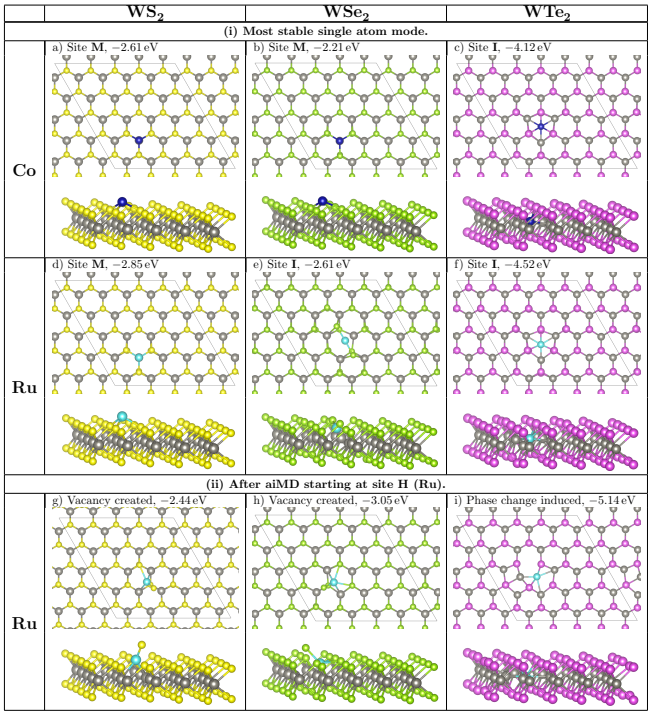


Figure 2: Single-atom adsorption on WX_2. (i) Most stable single atom sites for Co on (a) WS_2, (b) WSe_2, (c) WTe_2, and Ru on (d) WS_2, (e) WSe_2, (f) WTe_2. (ii) Ru structures after relaxing final frame of aiMD, where the monolayer is altered by chalcogen migration ((g) WS_2, (h) WSe_2) or a local phase change ((i) WTe_2). Co atoms do not alter the monolayer during the course of relaxation. Only one migration is seen for Co and its path is shown in figure 5. $E_{bind/atom}$ in eV. Colours: blue = Co; cyan = Ru; grey = W; yellow = S; green = Se; purple = Te.

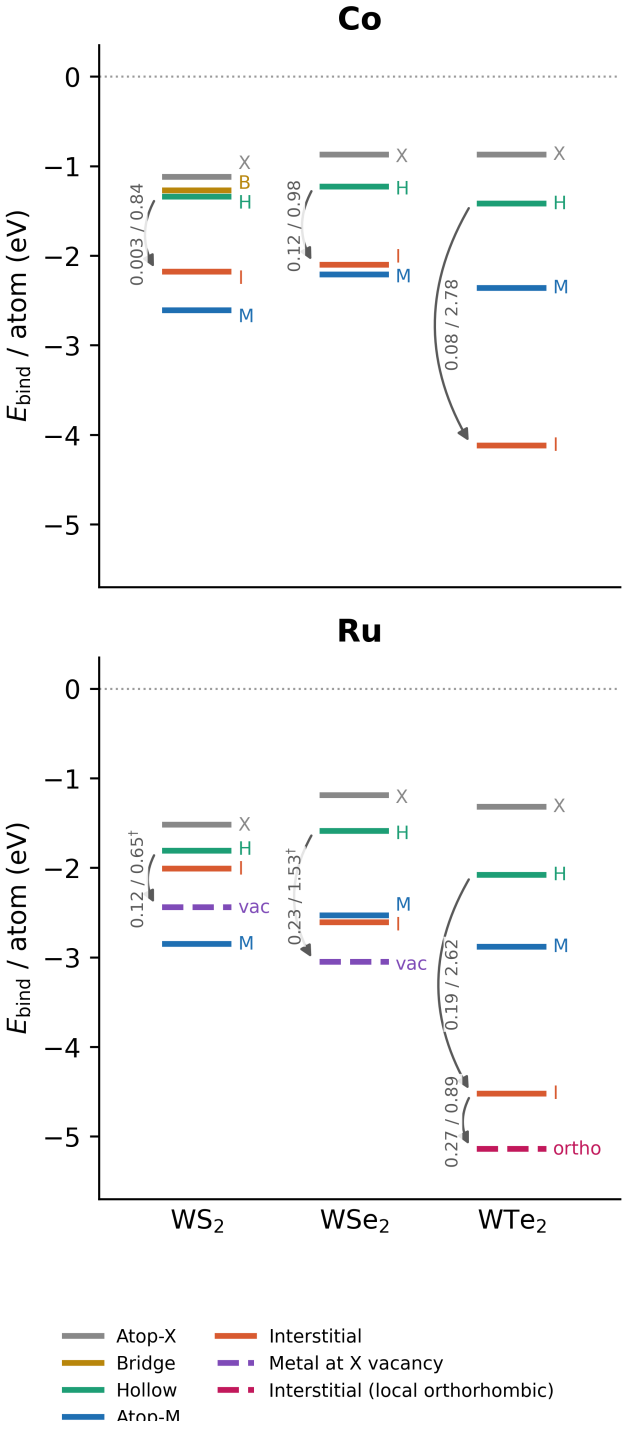


Figure 3: Schematic showing relative energies of sites, and activation barriers between sites for single atom Co (top) and Ru (bottom) structures. Arrows display the forward and reverse NEB barriers, with largest barrier shown for two step processes (denoted by †). "vac" denotes the metal occupying a chalcogen-vacancy site and "ortho" the interstitial site in the locally orthorhombic structure.

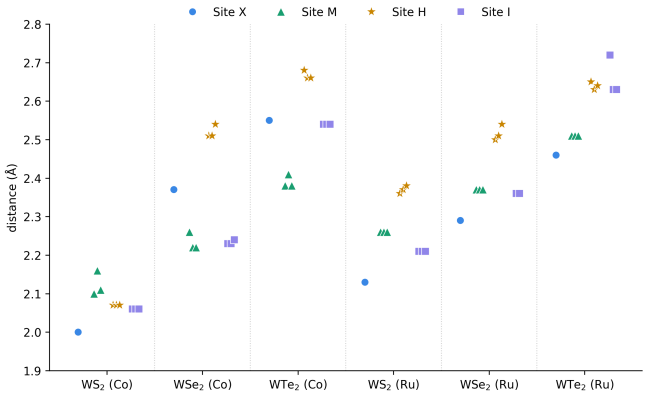


Figure 4: Adatom-chalcogen distances for single atom adsorption.

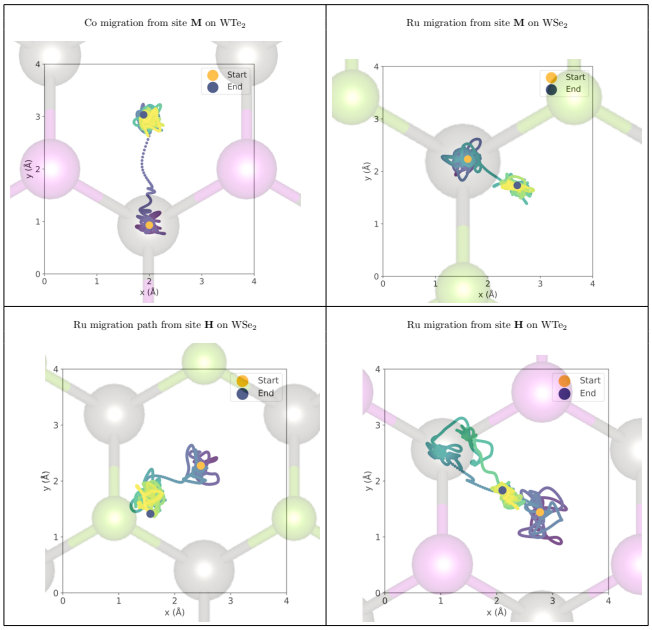


Figure 5: Plot of the migration path for single Co and Ru adatoms in the aiMD simulations. Specifically Co at site **M** on WTe_2 (top left), Ru at site **M** on WSe_2 (top right), Ru at site **H** on WSe_2 (bottom left), and Ru at site **H** on WTe_2 (bottom right).

grates away from the TMD layer, forming a vacancy. The Ru atom then migrates to occupy this vacancy site, with the chalcogen lying on top of Ru, see figure 2 (g) and (h). On WS_2 this occurs within 1.5 ps. However, on WSe_2, Ru remains stable at the **hollow** site for approximately 5 ps before the selenium migrates and Ru substitutes the chalcogen at its original site. The energy required to form a selenium vacancy on WSe_2 is 0.33 eV larger than for a sulphur vacancy on WS_2 and this is likely why the Ru atoms persists at the **hollow** site before selenium migrates for longer on WSe_2, compared to WS_2. Upon relaxation, Ru remains at the chalcogen site on WS_2 and this has a binding energy of -2.44 eV, thereby forming the second most stable single atom adsorption mode for Ru on WS_2, with Ru at site **M** being more stable by 0.41 eV. For Ru on WSe_2 however, the relaxed Ru atom at the vacancy site has a binding energy of -3.05 eV, making it the most stable Ru adatom adsorption mode on WSe_2. This structure is 0.44 eV more stable than adsorption of Ru at site **I**.

From NEB calculations we see that the formation of these vacancies requires two transition states before forming the final structure, with the forward barriers on WS_2 being 0.06 and 0.12 eV, and the reverse barriers being 0.65 and 0.16 eV. For Ru on WSe_2 we find the forward barriers are 0.23 and 0.07 eV, and the reverse barriers being 1.53 and 0.23 eV respectively, see Fig. 3.

On WTe_2 Ru also stays adsorbed at site **H** for approximately 5 ps. Rather than migrating directly to form an interstitial, it migrates to an adjacent site **M** where the adatom remains for 2.5 ps. After this, the tungsten atom underneath the Ru adatom displaces from its initial position, to form a locally orthorhombic structure. This thereby creates a large void into which the Ru atom migrates, taking an **interstitial** site. Upon relaxation, this structure has a binding energy of -5.14 eV, making it the most stable adsorption structure for Ru on WTe_2, see figure 2 (i). We find that the energy barrier required to induce local transition from the metastable hexagonal, to an orthorhombic structure is 0.27 eV, with the reverse process having an activation barrier of 0.89 eV.

Simulation of single metal adatoms at finite temperature reveals that, on all three monolayers, it is energetically advantageous for the metal atom to modify WX_2, either via the formation of chalcogen vacancies or altering of the local crystal structure at typical back-end-of-the-line temperatures. Such dynamics are not captured by 0 K DFT relaxations.

3.2 Two atom adsorption

Two atom clusters represent the very start of metal film growth on these monolayers, from which the initial competition between metal-metal, and metal-substrate energies can be investigated. By comparing adsorption stability of **neighbouring**, **non-equivalent**, and **separated** geometries, the interplay between the range of adsorption sites, presence or absence of adatom-adatom bonds, and

their effect on final binding energies can be established.

Three different initial configurations were considered for two atom adsorption. The first configuration, labelled as **Neighbouring**, has metal atoms adsorbed at nearest neighbour equivalent sites, allowing the adatoms to form a metal-metal bond. The second configuration, labelled as **Separated**, has metal atoms arranged at equivalent third nearest neighbour sites with no metal-metal adatom bonds. The final configuration, labelled **Non-Equivalent**, has metal atoms located at second nearest neighbour non-equivalent sites in differing permutations (**X-M**, **X-H**, **X-I**, **M-H**, and **M-I**). All 2 atom structures are shown in figures S4-S9 of the Supporting Information, with the most stable structures shown in figure 6.

For two atom clusters, both metal-metal and metal-substrate interactions play an important role in the overall stability. This is similar to the behaviour of Co and Ru on MoS_2, where both the metal adsorption site and the presence or absence of metal-metal bonds were key in determining final adsorption site stability[57]. For Cu on WX_2 however, only the metal-metal energy played a significant role in determining the stability of 2 atom clusters[40]. For both metals and all monolayers, except Co on WS_2, **neighbouring** adsorption at interstitial site **I** is the most stable two atom adsorption structure. In this adsorption mode, both the metal-substrate, and metal-metal energies can be maximised due to both large metal-metal and metal-monolayer interactions for **neighbouring** structures at site **I**.

For all metal-monolayer combinations, **separated** adsorption at site **X** is the least stable adsorption mode. For this adsorption mode, both the metal-substrate energy and metal-metal interaction energy remain small due to the separation of the metal adatoms, each of which has only a single metal-substrate bond.

By comparing **separated** and **neighbouring** adsorption at site **X**, the effect of metal-metal bonds on adatom stability can be demonstrated. **Neighbouring** adsorption modes at site **X** are $\sim$ 1 eV more favourable for Co, and $\sim$ 1.5 eV more favourable for Ru compared to **separated** metal atom adsorption at site **X**. This increase in binding energy is solely due to an increase in the metal-metal interaction energy caused by the metal bond present in **neighbouring** structures, which is absent in **separated** adsorption modes. The Co-Co and Ru-Ru bonds are shortest for **neighbouring** adsorption at site **X**, and longest at site **M**, see table 2. This demonstrates that, although the adsorption site remains the most important factor in stability, the metal-metal bonds also play a significant role in overall adatom stability, partic-

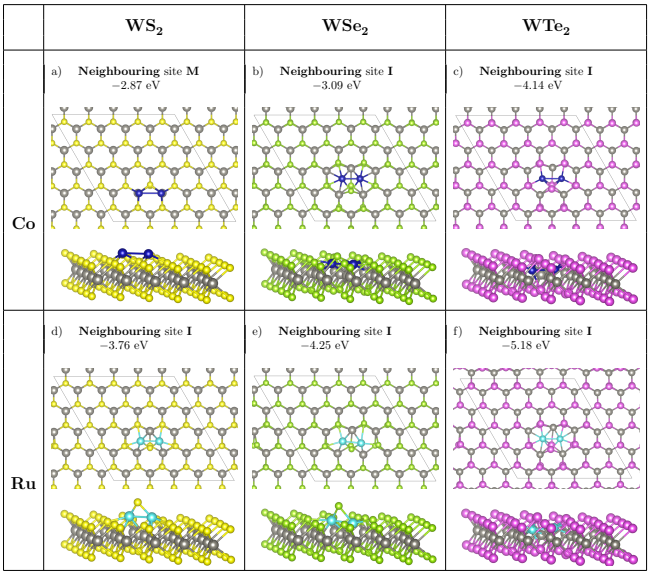


Figure 6: Most stable 2 atom adsorption modes: Co on (a) WS_2, (b) WSe_2, (c) WTe_2, and Ru on (d) WS_2, (e) WSe_2, (f) WTe_2. Ru shows a preference for adsorption at site **I**, making chalcogen atoms migrate from their original site on WS_2 and WSe_2. $E_{bind/atom}$ shown in eV in this figure. Atomic colours are as follows: blue = Co; cyan = Ru; grey = W; yellow = S; green = Se; purple = Te.

ularly at the less favourable single atom adsorption sites.

Table 2: Metal–metal distances for neighbouring adsorption modes.

	Monolayer	X (Å)	M (Å)	H (Å)	I (Å)
Co	WS_2	2.13	2.88	–	2.84
	WSe_2	2.26	2.99	–	2.45
	WTe_2	2.26	3.38	–	2.83
Ru	WS_2	2.15	2.76	2.22	2.47
	WSe_2	2.12	2.75	2.21	2.54
	WTe_2	2.12	2.83	2.23	2.68

Absent entries correspond to structures that relaxed to a different final geometry from the neighbouring starting configuration.

Although **neighbouring** adsorption at site **X** is ~ 1 eV more favourable compared to **separated** for Co adsorption, this structure is the second least stable 2 atom structure on WS_2 and WTe_2, and the third least stable structure on WSe_2. In spite of the large increase in binding energy arising from the Co dimer with a metal-metal bond, the adsorption of Co atoms at the unfavourable site **X** causes the overall binding energy to remain smaller than the other Co dimer adsorption modes at other sites. Furthermore, **separated** Co modes at sites **I** and **M** have competitive binding energies to both **neighbouring** and **non-equivalent** modes at less favourable sites **X** and **H**. This is due to the fact that the metal-substrate interaction energy, and therefore adsorption site, has the largest effect on the overall binding energy for Co adsorption onto WX_2.

For Ru however, this increase in metal-metal interaction energy has a much larger effect on adsorption stability. **Neighbouring** adsorption at site **X** displays an intermediate stability for Ru adsorption on the three monolayers, rather than being one of the least stable structures. In general, the difference in binding energy for **separated** and **neighbouring** modes is much larger for Ru than for Co, due to the greater affinity for Ru to maximise the metal-metal interaction energy which arises from the larger cohesive energy of Ru (-6.99 eV) compared to Co (-5.19 eV). This suggests that metal-metal interaction and adsorption site together determine the stability of Ru on WX_2, as a distinct preference for sites **M** and **I** over **X** and **H** remain, irrespective of metal-metal bonding.

As with single Co atom adsorption, site **M** is the most stable site on WS_2 for a Co dimer. For Ru however, site **M** is no longer the most stable site for **neighbouring** adsorption; rather, site **I** becomes the most stable site for **neighbouring** adsorption of Ru on WS_2. This is due to the migration of sulphur upon Ru dimer adsorption and relaxation, which allows the Ru atoms to arrange more favourably within the monolayer such that the lattice constant of WS_2 no longer limits the metal-substrate binding at site **I**. This again shows that adsorbed Ru atoms may promote chalcogen migration, leaving a vacancy in the monolayer to be filled by a metal adatom which increases the overall adsorption stability. This adsorption mode of Ru also forms a sulphur vacancy on MoS_2[57].

From equation 6, we find that the chalcogen vacancy formation energy for MoS_2, WS_2, WSe_2, and WTe_2 are 2.33, 2.49, 2.82, and 3.15 eV respectively. Therefore, the energy required to form a sulphur vacancy is 0.16 eV smaller on MoS_2 than it is on WS_2, and therefore the general propensity for Ru to promote sulphur migration and form vacancies is larger on MoS_2.

Figure 6 (e) shows that the **neighbouring** configuration of the Ru dimer at site **I** on WSe_2 also promotes chalcogen migration, forming a vacancy. This is in contrast to the behaviour of Co for this adsorption mode, where no selenium migration is observed. This behaviour again arises from the atomic radius of Ru being larger than the radius of Co, meaning it occupies a much greater volume than Co. Selenium migration allows both Ru atoms to occupy the most favourable adatom site, namely site **I**.

For **separated** adsorption of both Co and Ru onto WS_2, only adsorption at site **M** was competitive with **neighbouring** dimers. This behaviour is also seen on MoS_2 where only **separated** adsorption at site **M** was competitive in energy with clusters containing a metal bond. For Co on WS_2, this adsorption mode forms the third most stable structure, whereas for Ru, it is one of the least stable structures, again showing that the adsorption site plays a larger role in adatom stability for Co than for Ru.

The **separated** adsorption of Ru at site **I** on WTe_2 has a significantly larger binding energy compared to other **separated** and **neighbouring** Ru adsorption modes. The large binding energy here in comparison to other **separated** Ru structures in particular, is largely due to the larger lattice constant of WTe_2 compared to those of WS_2 and WSe_2. Therefore, the distortion energies do not compete with the increase in metal-substrate interaction energy for Ru to adsorb at site **I** on WTe_2. Furthermore, the metal-substrate energy is larger on WTe_2 compared to WS_2 and WSe_2 and so the combination of

these two factors greatly enhances the adsorption stability of **separated** adsorption at site **I** on **WTe2**. This does not negate Ru's preference for metal-metal bonds over metal-surface bonds as the other **separated** adsorption structures on WTe_2 are generally not as stable as Ru adsorption modes with a metal-metal bond present.

WTe_2 tends to have the most stable adsorption modes for both metals, followed by WS_2, and then WSe_2, a trend we also observed for Cu[40]. The range of adsorption energies is also quite different on each monolayer, with the difference between most and least stable adsorption structures being 2.74, 3.38, and 4.31 eV for the sulphide, selenide and telluride respectively. Similar to single atom adsorption, these differences arise from the behaviour of adsorption at the **interstitial** site on each monolayer. WTe_2 is able to incorporate both Ru and Co at this site with minimal strain, allowing for a very large binding energy compared to its least stable structure. As the size of the chalcogen decreases for both selenium and sulphur, the energy gain for interstitial adsorption, largely due to an increasing distortion energy at this site, reduces dramatically, leading to a smaller range of adsorption energies.

3.3 Four atom adsorption

Four different starting structures were considered for the 4 atom nanocluster adsorption. Two structures labelled **Line** and **Rhombus** are initially 2D (all metal atoms interact with the TMD monolayer), and the two starting structures labelled **3D-Rectangle** and **Tetrahedron** are 3D, in which at least one metal atom does not interact at the TMD monolayer. All relaxed structures for 4 atom nanocluster adsorption are shown in Figures S10 - S15 of the Supporting Information. The most stable structures are shown in figure 7.

For adsorption of 4 atom Co nanoclusters onto WS_2, 3D structures are the most stable. Specifically, the **tetrahedron** structures adsorbed at site **M** are the most favourable Co nanoclusters on WS_2, as these structures promote both the large metal-metal and metal-substrate interaction energies. The most stable of these structures, with a binding energy of -3.37 eV, promotes sulphur migration to form a sulphur vacancy in the monolayer, which a Co atom then occupies. This tetrahedron structure is ~ 0.2 eV more stable than those **tetrahedron** structures at site **M** which do not show sulphur migration (see figure S10).

Although these **tetrahedron** structures are the most stable on WS_2, it should be noted that Co does not in fact show a clear preference for either 2D or 3D structures on WS_2. Both 2D and 3D adsorption structures remain competitive in stability, with the most stable 2D structure, the **rhombus** adsorption at site **M**, having an adsorption energy of -3.08 eV. Furthermore, this structure does not cause any sulphur migration. Although the most stable structure is 3D, the least stable adsorption structure is also a 3D structure. Namely, the **3D-rectangle** at site **X** has the smallest binding energy of -2.49 eV. This is similar to Co on MoS_2, where there is a slight preference for 3D structures, but in general 2D and 3D structures have similar stability, suggesting no clear preference for either morphology for small nanoclusters.

Similar behaviour is found for Ru on WS_2, where the **tetrahedron** structure adsorbed at site **M** is the most favourable structure, with a binding energy of -4.18 eV. As with Co, both 2D and 3D Ru structures are competitive in energy on WS_2. Because the metal-metal interaction has a stronger effect on Ru adsorption, the preference for 3D adsorption modes is stronger compared Co. For Ru on WS_2 the least stable adsorption mode is the 2D **line** at site **X**, with a binding energy of -3.30 eV. Similar stability ranges for 2D and 3D structures were also observed for adsorption of Ru onto MoS_2, suggesting similar behaviour of Ru on the TMD selenides.

Although Ru shows a preference for 3D over 2D adsorption on WS_2, there are 2D structures which are more stable than some 3D modes. The **line** structure at site **H** on WS_2 has an adsorption energy of -3.86 eV (see figure 8). In this structure sulphur has migrated, thereby greatly increasing the metal-substrate energy for Ru nanocluster adsorption. For all cluster sizes we see the adsorption of Ru is greatly enhanced in stability when chalcogens migrate, leaving a vacancy in the TMD monolayer. This may promote intermixing of the metal and TMD that can be beneficial for, e.g. TMD-metal contacts. The distance between the Ru adatoms and the sulphur atom which has migrated from its original site, which is 2.20 Å, is slightly shorter than the Ru-S distance in bulk RuS_2 which is 2.37 Å[76]. Furthermore, the presence of the chalcogen vacancies may promote a 2D morphology for Ru on WX_2.

The behaviour of Ru on all TMD monolayers is consistent; the **Tetrahedron** structure at site **M** is always the most stable Ru nanocluster adsorption geometry. For adsorption onto all three monolayers, there is in general a clear preference for 3D clusters, particularly those adsorbed at site **M**. This arises from Ru having a preference for maximising metal-metal interaction energies, resulting in a preference for 3D clusters.

No chalcogen migration and vacancies are observed af-

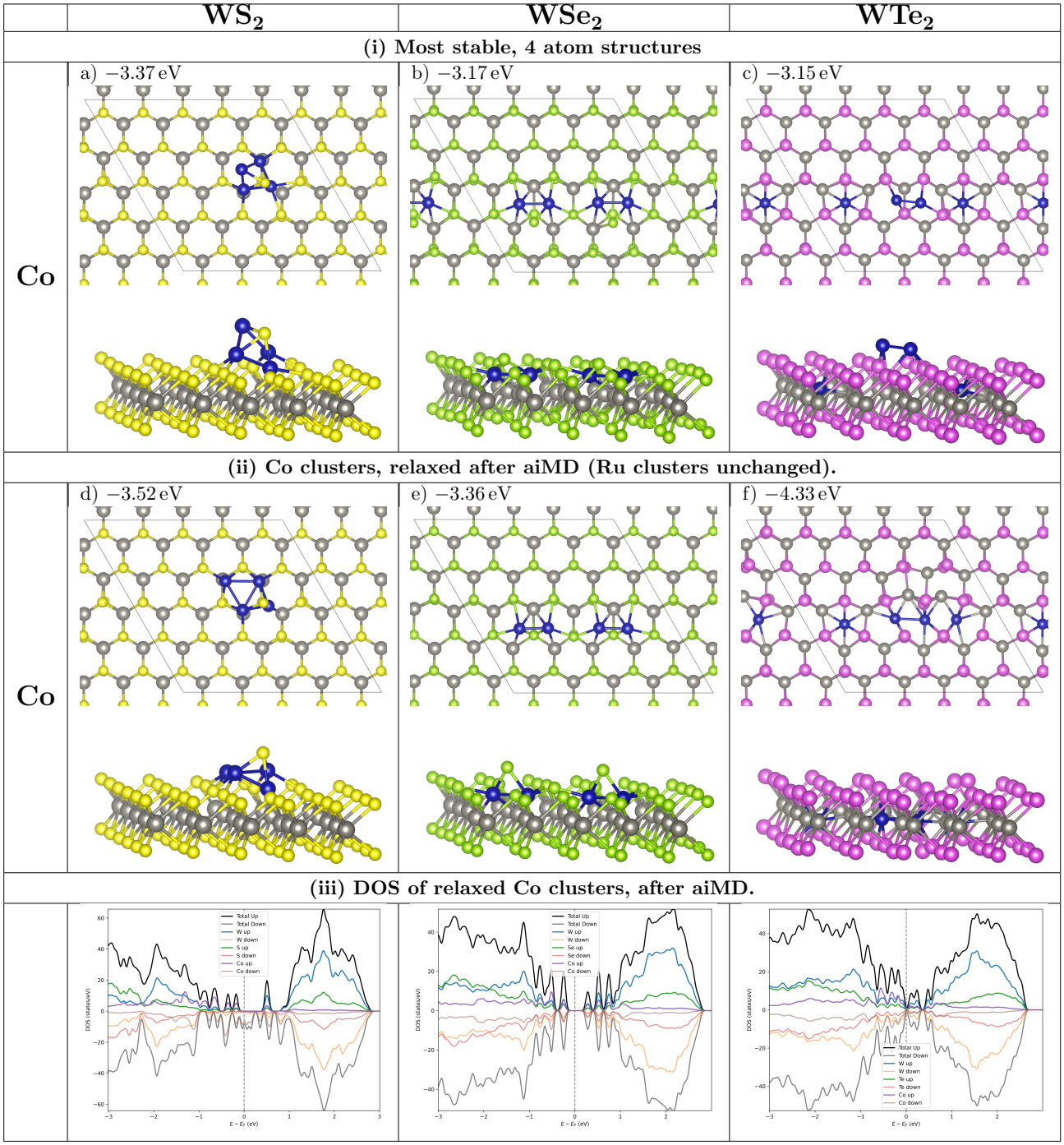


Figure 7: Four-atom adsorption. (i) Most stable Co 0 K structures on (a) WS_2, (b) WSe_2, and (c) WTe_2. (ii) Co structures after 500 K aiMD on (d) WS_2, (e) WSe_2, and (f) WTe_2. The tetrahedron transitions to 2D (WS_2), Se vacancies form (WSe_2), and WTe_2 distorts to a local orthorhombic phase. Ru clusters do not alter the monolayer or transition to alternative structure during aiMD, see figure 8. (iii) Total DOS of relaxed structures, after aiMD. $E_{bind/atom}$ in eV. Colours as in Fig. 2.

ter Ru nanocluster adsorption on the WSe_2 or WTe_2 monolayers. Additionally, more sulphur vacancies form on MoS_2 than do on WS_2. This is due to MoS_2 having the smallest sulphur vacancy formation energy of these four monolayers, followed by WS_2, then WSe_2, and finally WTe_2. The increase in vacancy formation energy on the selenide and telluride, combined with the inherent stability of the **tetrahedron** structure due to its large metal-interaction energy, makes it unfavourable for Ru to form vacancies on these monolayers unlike the behaviour seen for 1 and 2 atom clusters on WS_2 and WSe_2. The enhanced stability of 4 atom Ru clusters over smaller clusters arises from the large metal-metal interaction energies and is also likely why no Ru atom is present at an **interstitial** site, despite this adsorption mode being very favourable for Ru in both 1 and 2 atom adsorption.

The behaviour of 4 atom Co structures is similar on WSe_2 and WTe_2 monolayers. For both the selenide and telluride, structures which have Co atoms adsorbed at site **I** form the most stable structures. In particular, **line** structures where Co atoms are initially at site **H**, form the most stable mode on both WSe_2 and WTe_2 with a binding energy of -3.17 and -3.15 eV respectively. On WSe_2, all Co atoms are at site **I**, whereas on WTe_2 only two atoms are at site **I**. The remaining 2 Co atoms are adsorbed at the surface at site **H** and **B**, with a Co-Co distance of 2.19 Å. The atoms at site **H** and **B** form a dimer whereas the atoms at site **I** are isolated.

If structures with Co atoms adsorbed at site **I** are excluded from analysis, then an energetic preference for 3D over 2D structures of Co can be seen. As with Ru, this is due to the increased lattice parameter of both of WSe_2 and WTe_2 which leads to an increase in the Co-Co distance for 2D structures. This increased Co-Co distance leads to a reduction in the strength of the metal-metal interaction energy for 2D clusters to such an extent these structures are no longer as competitive with 3D structures, as they were on WS_2. This can be seen most clearly by comparing the **line** structure at site **M** on WS_2 and WTe_2. Both these Co structures have the same geometry, except for the distance between the Co atoms adsorbed at site **M**. On WS_2 the average inter Co-distance for this structure is 3.09 Å, corresponding to a metal interaction energy of -1.00 eV. On WTe_2, this distance increases to 3.49 Å, and has a decreased metal interaction energy of -0.66 eV.

aiMD calculations were performed for the most stable 4 atom structure of each metal-monolayer combination. For Co on WS_2, the introduction of temperature drives a change in morphology from 3D to 2D. After $\sim$ 1.25 ps, the Co atom at the apex of the tetrahedron migrates

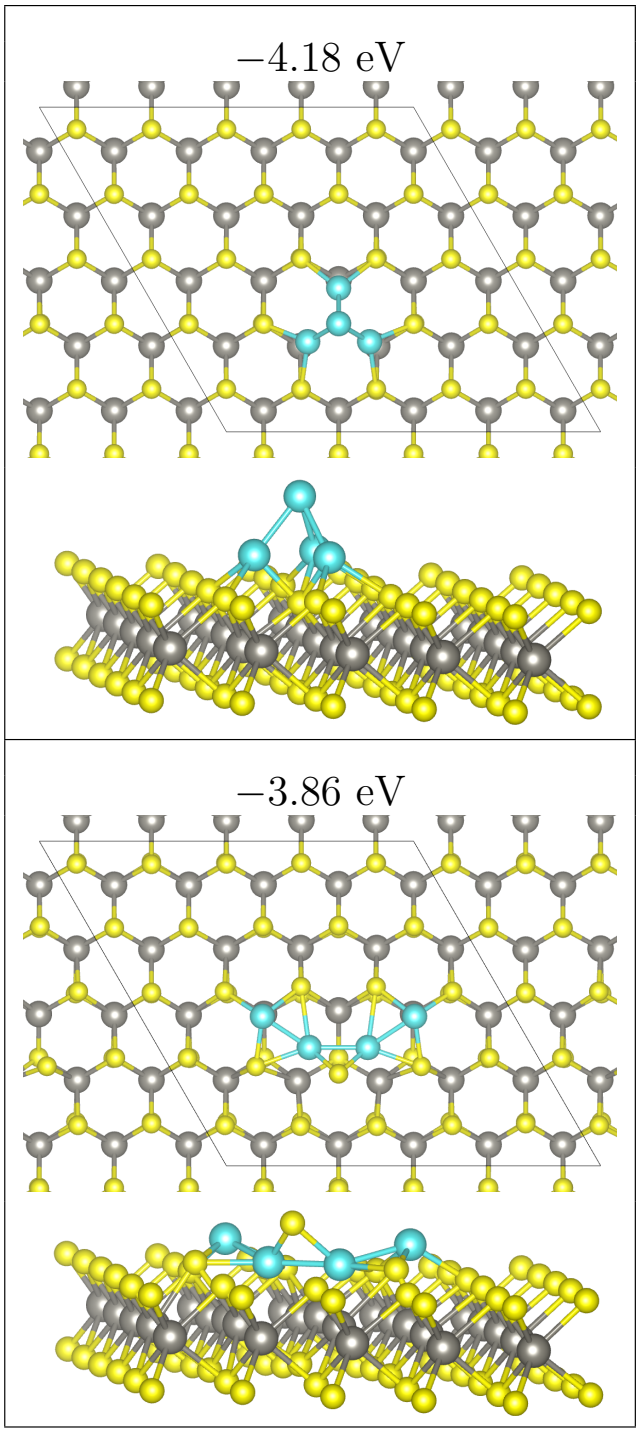


Figure 8: Examples of Ru adsorption structures containing 4 atoms. Tetrahedron adsorption structure at site **M**, the most stable Ru 4 atom structure on each monolayer (top). Ru structure forming a sulphur vacancy (bottom).

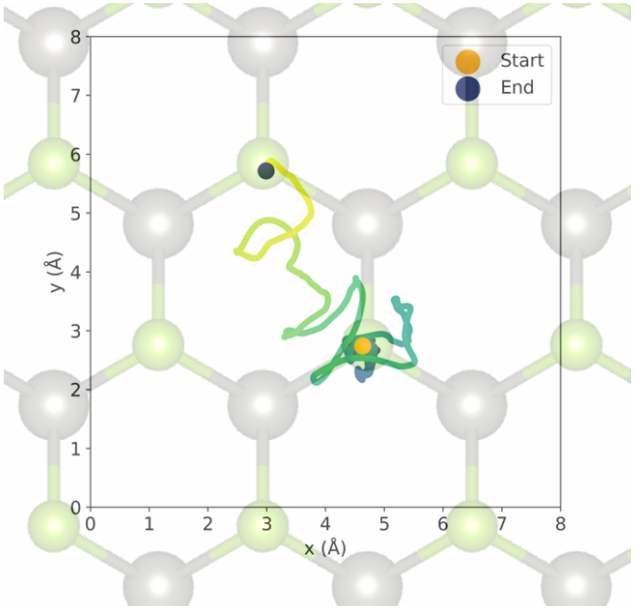


Figure 9: Migration path of the centre of mass of Ru **tetrahedron** from 15 ps aiMD simulation on WSe_2.

to adsorb directly on the monolayer. It is initially at a **Bridge** site. Then after a further ~ 1.25 ps, it migrates to an adjacent site **M** and remains there for the rest of the aiMD. All other metal atoms in the cluster remain at their interaction site - the most stable **M** site - on the WS_2 over the course of the aiMD.

The final frame of the MD was then relaxed and the computed binding energy is -3.52 eV, which is 0.15 eV more stable than the DFT relaxed structure. This once again shows that both 2D and 3D morphologies have competitive binding energies for a range of Co nanocluster adsorption structures. It also further indicates that the presence of chalcogen vacancies can promote 2D cluster morphology, but that temperature also plays a key role in the preferred nanocluster structures.

This also highlights that dynamic behaviour of adsorbed metal nanoclusters is critical as the exploration of a wider configuration space with even short dynamics simulations can lead to new and more favourable adsorption modes that are not accessible to 0 K relaxations; the latter would indicate that Co adsorption on WX_2 has a slight preference for 3D morphology.

The initial structure of Co on WSe_2 has all atoms adsorbed at **interstitial** sites on the monolayer. The introduction of temperature to this structure does not cause the Co atoms to migrate from these sites, with 4 Co atoms arranged as two Co dimers, with Co-Co distances of 2.48 and 2.46 Å initially at **interstitial** sites throughout the simulation. Two selenium atoms neighbouring each Co dimer migrate above the Co atoms over the course of the aiMD, leaving two vacancy sites in the monolayer, see figure 7 (e). The first selenium starts migrating after 3.5 ps, with the second migrating after 7.5 ps. These selenium atoms then remain near the Co dimers during the remainder of the simulation. The final frame of this structure was also relaxed and has an adsorption energy of -3.36 eV, which is 0.19 eV more stable than before the chalcogen vacancies were formed. Although this energy gain is small, the vacancy formation through chalcogen migration can have a strong influence on morphology and film quality, especially if chalcogen atoms intermix into the metal thin film.

Co on WTe_2 has two Co atoms present at the **interstitial** sites, with the other two Co atoms adsorbed on the monolayer at sites **H** and **B**. After ~ 1.8 ps of the aiMD, the atom at **B** migrates to the neighbouring site **M**. Similar to single atom aiMD of Ru on WTe_2, the migration of Co to this site then causes the displacement of the tungsten atom under this Co atom to form a locally orthorhombic structure. This allows both atoms initially on the monolayer to migrate to **interstitial** sites after ~ 2.5 ps. Interestingly, from $\sim 4-5$ ps after the start of the aiMD, this tungsten atom then returns to its original site, thereby transitioning from orthorhombic back to the original hexagonal structure. After 5 ps however, two tungsten atoms neighbouring the Co atoms at sites **I** displace from their hexagonal position to again form a locally orthorhombic structure for the remainder of the aiMD. The displacement of two tungsten atoms forms a large void in the monolayer in which the Co atoms reside. The dynamics then promote atom migrations that open up the WTe_2 monolayer to incorporate Co atoms.

The final frame of this simulation was relaxed and has an adsorption energy of -4.33 eV, 1.18 eV more stable than the initial relaxed structure. This is far more stable than any other Co structure found on WTe_2 indicating that at typical process temperatures, Co clusters may not be stable on 2H-WTe_2, but rather may cause local distortions in the monolayer, changing the structure from hexagonal to orthorhombic near the Co clusters.

On all monolayers the most stable Ru nanocluster was a **tetrahedron** adsorbed at site **M**. On WS_2 and WTe_2, this cluster remains adsorbed at this site for the entire simulation, with no clear atom migrations from the monolayer. On WSe_2, the Ru cluster remains at its initial site for ~ 8.5 ps, after which point it begins to migrate across the monolayer. As it migrates, the cluster itself begins to rotate so that it "rolls" across the monolayer.

This difference in behaviour between the three monolayers likely occurs as adsorption energy of this cluster to the selenide monolayer is ~ 0.3 eV smaller compared to the same cluster on the sulphide or telluride monolayer.

Although we have shown that single adatoms and dimers of Ru have a propensity to adsorb at site **I** and promote chalcogen migration, this is not seen in the dynamics of these tetrahedron 4-atom nanoclusters. This arises from the very large metal-metal interaction energies of the tetrahedron structure maintaining the cluster structure, and the barrier to form vacancies or dissociate the cluster is not overcome at this temperature or timescale. Exploring longer time dynamics would require machine learning simulations or classical molecular dynamics which are beyond the scope of this work.

3.4 Bader Charge Analysis, Electronic Density of States, and Evolution of Magnetic Moments

Computed Bader charges for examples of metal adatom adsorption and metal nanocluster adsorption are shown in table 3. The Bader charges show that the charge transfer behaviour of both metals is largely dependent on the monolayer to which the metal atoms are adsorbed. For WS_2 structures in which sulphur migrates off the lattice site (denoted by "vac", table 3), Co and Ru are oxidised, with a charge transfer of 0.4 and 0.2 electrons to the monolayer. On the selenide and telluride in the most stable **I** site, Ru is partially reduced.

For the 4 atom nanocluster, Co on the selenide monolayer shows little charge transfer and Ru on the sulphide shows partial oxidation of the three metal atoms bound to the monolayer, while the apex atom remains metallic. This behaviour is typical for adsorbed tetrahedron clusters[39,57]. Finally, for Co on WS_2 with sulphur migration, there is clear oxidation of the Co atoms, with changes in charge of -0.2 or -0.4 electrons.

From density of states calculations (Supporting Information Table S7), we see that adsorption of metal atoms leads to the formation of local electronic states within the energy gap of each TMD monolayer. From the example of Co adsorbed onto WS_2 in figure 10, we see that the adatoms introduce states crossing the Fermi level for structures that both do and do not induce a sulphur migration out of the monolayer. This likely arises due to WS_2 partially oxidising the adsorbed Co atoms and is in line with our previous work on Cu, Co and Ru adsorption on MoS_2[39,57]. The band edges of each monolayer are not affected however. From figure 10, we see that this is only a local perturbation of the monolayer with the density of states for atoms remote (further than 5 Åfrom adatoms) from the nanocluster being unaffected. Furthermore, excepting the new localised states, the overall valence and conduction band structures are unaffected when comparing to those of the pristine monolayer (figure S16). This demonstrates that adsorption of Co onto these monolayers can induce local metallisation which is important for carrier injection, without having an adverse effect on the overall semiconducting properties of the WX_2 monolayer.

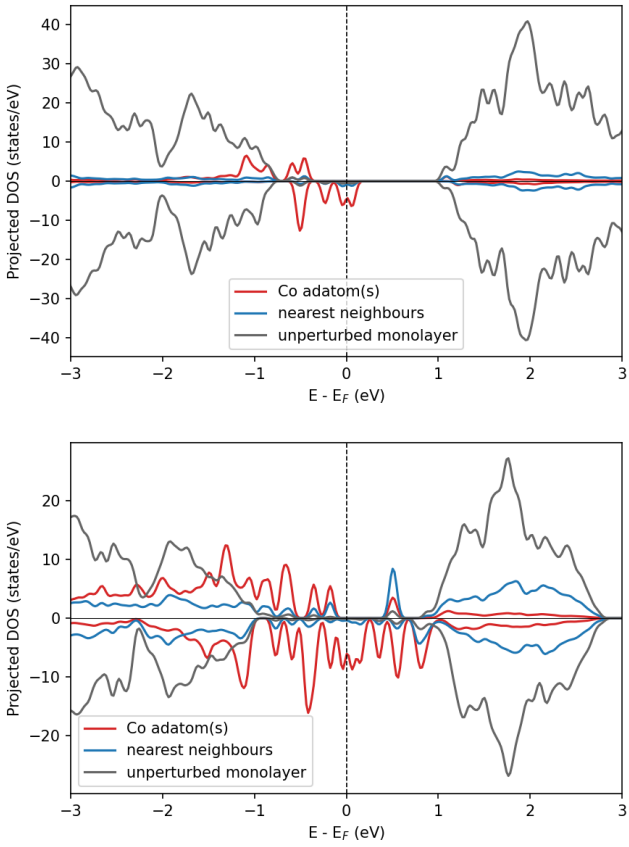


Figure 10: Total (summed over all orbitals) projected density of states of Co adatoms, nearest neighbours, and atoms far from the adsorbed Co atoms. Although Co atoms induce states crossing the Fermi level, this is only a local perturbation. DOS corresponds to **Co-S-M** (top, figure 2 (a)) and **Co-S-Htet-vac** (bottom, figure 7 (a)).

Table 3: Change in Bader charge ΔQ for selected adsorption structures.

Structure	Atom 1	Atom 2	Atom 3	Atom 4
Single metal adatom				
Co-S-M	−0.4			
Ru-Se-I	0.1			
Ru-Te-I	0.4			
Ru-S-I-vac	−0.2			
Four-atom nanocluster				
Co-S-Htet-vac	−0.4	−0.2	−0.4	−0.4
Co-Se-Hline	0.1	0.1	0.0	0.1
Ru-S-Mtet	−0.2	−0.2	−0.2	0.1

$\Delta Q = Q_{\text{bader}} - Q_{\text{valence}}$, the change in Bader charge relative to the neutral-atom valence (electrons). Structures are labelled Metal-Chalcogen-Site; "vac" denotes a chalcogen migrated from its lattice site; "tet" and "line" the **tetrahedron** and **line** geometries. For nanoclusters ΔQ is given per metal atom.

3.4.1 Spin behaviour

We explore the relationship between spin state and atomic moment for both Co and Ru. Total magnetic moment for single atom adsorption can be found in table 4, with the atom projected moments for these structures in tables S8 and S9. As the WX_2 monolayers do not carry a moment on any atom, the net magnetic moment of each adsorption structure can be attributed to the metal species on the monolayer. For Co in particular, we also compare the adsorption energy of fully relaxed structures, to structures where the total magnetic moment has been fixed to a high spin state, where each Co atom has a total moment of 3 μ_B, as in a free Co atom.

For single atom adsorption (table 4), we find that the high spin state of Co is generally retained at weakly bound sites **X** and **H**. At strongly bound states **M** and **I** the total magnetic moment of Co is lowered to $\sim 1\mu_B$. When comparing the adsorption energy of these configurations to relaxation where the moment is fixed at $3\mu_B$, the low magnetic moment structures have a stronger adsorption energy of between 0.61 and 1.05 eV. Notably, Co at site **X** on WS_2 relaxes to have a moment of 1 $\mu_\mathbf{B}$ as opposed to 3 μ_B. The difference in energy between the low spin and high spin state is only 0.13 eV, much smaller compared to adsorption of Co at sites **M** or **I**. This is likely as the overall weaker bonding at this site means that a change in spin has a smaller effect on the overall binding energy. For single Ru atoms we find that the total moment on the Ru atom is 2 μ_B for sites where the Ru atom sits on the monolayer. For sites in which the Ru atom is in, rather than above, the monolayer the net moment on the atom is 0 μ_B. This occurs at site **I** on WSe_2 and WTe_2, or for structures where Ru generates a chalcogen vacancy and occupies the chalcogen site.

The correlation between total moment and adsorption site becomes less clear once cluster size increases. For dimer adsorption, total moment is still generally dependent on the sites the individual Co atoms occupy, however it is not directly correlated. For example, for separated Co atoms at site **X** on WTe_2, the total moment is 2 μ_B rather than the expected 6 μ_B, as is seen on WS_2 and WSe_2. Furthermore, these Co atoms have antiparallel moments. Similarly **separated** Co atoms at site **I** on WSe_2 have a total moment of 1.55 μ_B with antiparallel moments on each atom also. Ru dimers take on total moments of 0, 2 or 4 μ_B, all moments which arise from combinations of the possible single atom moments of Ru atoms (0 or 2 μ_B). Despite this there is not a clear correlation between adsorption site and total moment.

As with Co dimers, four atom Co clusters with both parallel and antiparallel moments are stable. The most stable 4 atom structure on WS_2 has ferrimagnetic-like ordering, with moments on each Co atom being 0.39, 0.38, 1.20, and −1.91 μ_B, with the negatively aligned moment corresponding to the apex Co in the tetrahedron. Once this structure is relaxed after aiMD, the moment on each atom is altered significantly, with 1.56, 1.46, 1.56, and 0.88 μ_B. This behaviour is also observed on WSe_2 and WTe_2, where clusters displaying ferromagnetic, ferrimagnetic, and antiferromagnetic-like structures are stable (table S8). From this we see there is not a clear relationship between local magnetic moment and adsorption site or nanocluster structure. However, a given nanocluster in which the spin is free to relax is generally more stable than clusters having a fixed high spin state. For Ru, all of the **tetrahedron** structures have a total moment of 2 μ_B, with the apex atom having the largest moment and the surface bound Ru atom's moment reduced greatly in comparison to single atom states (see table S9).

4 Conclusion

Understanding the fundamental interactions of metals adsorbed on transition metal dichalcogenides is crucial for enabling next generation technologies such as complementary field effect transistors or chemical catalysts. We have performed an extensive first principles DFT and ab initio Molecular Dynamics study of the adsorption, stability and dynamics of Co and Ru adatoms and small nanoclusters on WS_2, WSe_2, and WTe_2 monolayers. By

Table 4: Total magnetic moment of single-atom structures after relaxation.

	Site	WS_2 ($\lvert\mu_B\rvert$)	WSe_2 ($\lvert\mu_B\rvert$)	WTe_2 ($\lvert\mu_B\rvert$)
Co	X	1.00	3.00	3.00
	M	1.00	1.00	1.00
	H	3.01	3.00	3.01
	I	1.00	1.00	0.89
Ru	X	2.00	1.99	1.97
	M	2.00	2.00	2.02
	H	2.00	2.00	2.00
	I	2.00	0.00	0.00

investigating these metal-monolayer interactions at the atomic scale, we have uncovered factors which affect the initial stages of growth for Co and Ru films on tungsten TMD monolayers. By studying three monolayers we illustrate the role that the chalcogen and the TMD lattice parameter play in determining overall metal morphology. Finally, by comparing our results to previous work performed on Cu, Co, and Ru on MoS_2, and Cu on tungsten TMDs, we also gain insight into the role both adatom and metal monolayer species play.

Single atom adsorption shows that ionic radius of the adatom and lattice constant of the TMD both play a large role. On WS_2, the monolayer with the smallest lattice parameter, site **M** is the most stable adsorption site for all metals. As the lattice parameter increases, Co and Ru metal adatoms show an increasing preference for adsorption at the interstitial site **I**, which is facilitated by the relative size of the adsorbed metal and the TMD lattice.

As cluster size increases to multi-atom adsorption, we find that both metal-substrate and metal-metal interaction energy play a pivotal role in determining overall stability, unlike the behaviour seen with Cu on WX_2 where metal-metal adsorption energy was the dominant driving force for cluster stability. Although both energies play significant roles, we find that the influence of the metal-metal interaction is more significant for Ru adsorption compared to Co, likely arising from the larger cohesive energy of Ru compared to Co.

For both metals, we find that 2D and 3D nanocluster adsorption structures are competitive in stability from 0 K DFT relaxations. As Ru adatom stability is largely driven by metal-metal interaction energy, its preference for 3D adsorption structures is more pronounced than for Co. For Co adsorption there is a clear preference for 2D adsorption where atoms occupy site **I**, particularly on WSe_2 and WTe_2 as the lattice parameter of these monolayers is large enough to accommodate the atoms at this site.

Both metal atoms can promote chalcogen vacancy formation. While this behaviour was seen during 0 K relaxations, aiMD reveals that at typical back-end-of-the-line processing temperatures, both metals can promote chalcogen migration, creating vacancies in the monolayer. This migration can lead to an increase in the metal-substrate interaction energy and therefore can promote a 2D morphology. The metal adsorption-induced chalcogen migration may, however, undermine the monolayer's effectiveness as a barrier layer for interconnect structures. In contrast, this rearrangement could be beneficial for metal contacts as metal induced gap states may reduce contact resistance if such states are formed near band edges, rather than creating deep trap states. Both metal atoms can also cause local phase changes in hexagonal WTe_2 causing it to form a locally orthorhombic structure. For all three monolayers these adsorbed metals can greatly alter the structure of the monolayer either through vacancy formation, interstitial adsorption or local phase change.

Supporting Information

Single-, two-, and four-atom adsorption geometries for Co and Ru on WS_2, WSe_2, and WTe_2 monolayers; disaggregated adsorption energies for neighbouring, separated, non-equivalent two-atom, and four-atom configurations; average metal–chalcogen bond distances for single-atom adsorption; total and atom-projected magnetic moments for Co and Ru adsorption structures; spin-state energy differences between spin-relaxed and fixed high-spin states; electronic densities of states for selected Co and Ru structures; plane-wave energy cut-off convergence for the ab initio molecular dynamics calculations.

Acknowledgements

MS is supported by a Research Ireland (formerly Irish Research Council) Government of Ireland PhD Fellowship, Grant Number GOIPG/2023/4025. C-LN is supported by a Research Ireland (formerly Irish Research Council) Government of Ireland Postdoctoral Fellowship, Grant Number GOIPD/2025/976. MN is supported by the NanoIC Pilot Line (www.nanoic-project.eu). The acquisition and operation of NanoIC are jointly funded by the Chips Joint Undertaking, through the European Union's Digital Europe (101183266) and Horizon Europe

programs (101183277), as well as by the participating states Belgium (Flanders), France, Germany, Finland, Ireland and Romania. We acknowledge the Irish Centre for High End Computing (ICHEC) and LuxProvide for computing resources.

Conflicts of Interest

There are no conflicts of interest to declare.

Data Availability

The data underlying the results in this paper is available through the Zenodo repository at https://doi.org/10.5281/zenodo.21361426.

References

(1) Shanmugam, V.; Mensah, R. A.; Babu, K.; Gawusu, S.; Chanda, A.; Tu, Y.; Neisiany, R. E.; Försth, M.; Sas, G.; Das, O. A review of the synthesis, properties, and applications of 2D materials. Particle & Particle Systems Characterization **2022**, *39*, 2200031.

(2) Xiao, D.; Liu, G. B.; Feng, W.; Xu, X.; Yao, W. Coupled spin and valley physics in monolayers of MoS 2 and other group-VI dichalcogenides. Physical Review Letters **2012**, *108*, 196802.

(3) Cong, C.; Shang, J.; Wang, Y.; Yu, T. Optical Properties of 2D Semiconductor WS2. Advanced Optical Materials **2018**, *6*, 1700767.

(4) Mak, K. F.; Lee, C.; Hone, J.; Shan, J.; Heinz, T. F. Atomically Thin MoS2: A New Direct-Gap Semiconductor. Physical Review Letters **2010**, *105*, 136805.

(5) Mak, K. F.; He, K.; Lee, C.; Lee, G. H.; Hone, J.; Heinz, T. F.; Shan, J. Tightly bound trions in monolayer MoS 2. Nature Materials **2013**, *12*, 207–211.

(6) Radisavljevic, B.; Radenovic, A.; Brivio, J.; Giacometti, V.; Kis, A. Single-layer MoS2 transistors. Nature Nanotechnology **2011**, *6*, 147–150.

(7) Lopez-Sanchez, O.; Lembke, D.; Kayci, M.; Radenovic, A.; Kis, A. Ultrasensitive photodetectors based on monolayer MoS 2. Nature Nanotechnology **2013**, *8*, 497–501.

(8) Pu, J.; Yomogida, Y.; Liu, K.-K.; Li, L.-J.; Iwasa, Y.; Takenobu, T. Highly flexible MoS 2 thin-film transistors with ion gel dielectrics. Nano Letters **2012**, *12*, 4013–4017.

(9) Bertolazzi, S.; Brivio, J.; Kis, A. Stretching and breaking of ultrathin MoS 2. ACS Nano **2011**, *5*, 9703–9709.

(10) Kaplan-Ashiri, I.; Cohen, S. R.; Gartsman, K.; Ivanovskaya, V.; Heine, T.; Seifert, G.; Wiesel, I.; Wagner, H. D.; Tenne, R. On the mechanical behavior of WS2 nanotubes under axial tension and compression. Proceedings of the National Academy of Sciences of the United States of America **2006**, *103*, 523–528.

(11) Chhowalla, M.; Shin, H. S.; Eda, G.; Li, L. J.; Loh, K. P.; Zhang, H. The chemistry of two-dimensional layered transition metal dichalcogenide nanosheets. Nature Chemistry **2013**, *5*, 263–275.

(12) Silveira, J. F.; Besse, R.; Silva, J. L. D. Stacking Order Effects on the Electronic and Optical Properties of Graphene/Transition Metal Dichalcogenide Van der Waals Heterostructures. ACS Applied Electronic Materials **2021**, *3*, 1671–1680.

(13) Voiry, D.; Yamaguchi, H.; Li, J.; Silva, R.; Alves, D. C.; Fujita, T.; Chen, M.; Asefa, T.; Shenoy, V. B.; Eda, G.; Chhowalla, M. Enhanced catalytic activity in strained chemically exfoliated WS 2 nanosheets for hydrogen evolution. Nature Materials **2013**, *12*, 850–855.

(14) Tsai, C.; Chan, K.; Abild-Pedersen, F.; Nørskov, J. K. Active edge sites in MoSe2 and WSe2 catalysts for the hydrogen evolution reaction: A density functional study. Physical Chemistry Chemical Physics **2014**, *16*, 13156.

(15) Kwon, H.; Ji, B.; Bae, D.; Lee, J.-H.; Park, H. J.; Kim, D. H.; Kim, Y.-M.; Son, Y.-W.; Yang, H.; Cho, S. Role of anionic vacancy for active hydrogen evolution in WTe2. Applied Surface Science **2020**, *515*, 145972.

(16) Wang, Q.; Zhang, Q.; Luo, X.; Wang, J.; Zhu, R.; Liang, Q.; Zhang, L.; Yong, J. Z.; Wong, C. P. Y.; Eda, G.; Smet, J. H.; Wee, A. T. Optoelectronic Properties of a van der Waals WS2 Monolayer/2D Perovskite Vertical Heterostructure. ACS Applied Materials and Interfaces **2020**, *12*, 45235–45242.

(17) Barot, J. B.; Gupta, S. K.; Gajjar, P. Optical properties of WTe2-a layered topological insulator: A DFT study. Materials Today: Proceedings **2023, in press**, DOI: https://doi.org/10.1016/j.matpr.2023.01.191.

(18) Godel, F.; Zatko, V.; Carrétéro, C.; Sander, A.; Galbiati, M.; Vecchiola, A.; Brus, P.; Bezencenet, O.; Servet, B.; Martin, M. B.; Dlubak, B.; Seneor, P. WS22D Semiconductor down to Monolayers by Pulsed-Laser Deposition for Large-Scale Integration in Electronics and Spintronics Circuits. ACS Applied Nano Materials **2020**, *3*, 7908–7916.

(19) Wang, Z.; Zhao, L.; Mak, K. F.; Shan, J. Probing the Spin-Polarized Electronic Band Structure in Monolayer Transition Metal Dichalcogenides by Optical Spectroscopy. Nano Letters **2017**, *17*, 740–746.

(20) Xu, T.; Liu, Y.; Pei, Y.; Chen, Y.; Jiang, Z.; Shi, Z.; Xu, J.; Wu, D.; Tian, Y.; Li, X. The ultra-high NO2 response of ultra-thin WS2 nanosheets synthesized by hydrothermal and calcination processes. Sensors and Actuators, B: Chemical **2018**, *259*, 789–796.

(21) Guo, R.; Han, Y.; Su, C.; Chen, X.; Zeng, M.; Hu, N.; Su, Y.; Zhou, Z.; Wei, H.; Yang, Z. Ultrasensitive room temperature NO2 sensors based on liquid phase exfoliated WSe2 nanosheets. Sensors and Actuators, B: Chemical **2019**, *300*, 127013.

(22) Jha, R. K.; Bhat, N. Recent Progress in Chemiresistive Gas Sensing Technology Based on Molybdenum and Tungsten Chalcogenide Nanostructures. Advanced Materials Interfaces **2020**, *7*, 1901992.

(23) Liu, X.; Duan, G.; Li, W.; Zhou, Z.; Zhou, R. Membrane destruction-mediated antibacterial activity of tungsten disulfide (WS2). RSC Advances **2017**, *7*, 37873–37880.

(24) So, Y.; Yim, D. B.; Lee, S.; Lee, H.; Kim, H.; Yu, Y.; Choi, C.; Kim, J. H. Insights into the selective bactericidal activity of W(Mo)Se2 nanosheets for therapy of pathogenic bacterial infections. Chemical Engineering Journal **2023**, *468*, 143727.

(25) Sarakinos, K. A review on morphological evolution of thin metal films on weakly-interacting substrates. Thin Solid Films **2019**, *688*, 137312.

(26) Li, Y.; Liu, Q.; Shen, W. Morphology-dependent nanocatalysis: Metal particles. Dalton Transactions **2011**, *40*, 5811–5826.

(27) Yu, J.; Peng, G.; Peng, L.; Chen, Q.; Su, C.; Shang, L.; Zhang, T. Recent advancements in two-dimensional transition metal dichalcogenide materials towards hydrogen-evolution electrocatalysis. Green Energy & Environment **2025**, *10*, 1130–1152.

(28) Van der Straten, O.; Zhu, Y.; Rullan, J.; Dunn, K.; Kaloyeros, A. E. Study of copper-refractory metal interfaces via solid-state wetting for emerging nanoscale interconnect applications. Journal of Materials Research **2006**, *21*, 255–262.

(29) Peercy, P. S. The drive to miniaturization. Nature **2000**, *406*, 1023–1026.

(30) Brain, R. In 2016 IEEE International Electron Devices Meeting (IEDM), 2016, pp 9.3.1–9.3.4.

(31) Plombon, J.; Andideh, E.; Dubin, V. M.; Maiz, J. Influence of phonon, geometry, impurity, and grain size on copper line resistivity. Applied Physics Letters **2006**, *89*, 113124.

(32) Chawla, J.; Gstrein, F.; O'Brien, K.; Clarke, J.; Gall, D. Electron scattering at surfaces and grain boundaries in Cu thin films and wires. Physical Review B—Condensed Matter and Materials Physics **2011**, *84*, 235423.

(33) Gall, D. Electron mean free path in elemental metals. Journal of Applied Physics **2016**, *119*, 085101.

(34) Gall, D.; Cha, J. J.; Chen, Z.; Han, H.-J.; Hinkle, C.; Robinson, J. A.; Sundararaman, R.; Torsi, R. Materials for interconnects. MRS Bulletin **2021**, *46*, 959–966.

(35) Lo, C.-L.; Catalano, M.; Smithe, K. K.; Wang, L.; Zhang, S.; Pop, E.; Kim, M. J.; Chen, Z. Studies of two-dimensional h-BN and MoS2 for potential diffusion barrier application in copper interconnect technology. npj 2D Materials and Applications **2017**, *1*, 42.

(36) Lo, C.-L.; Zhang, K.; Smith, R. S.; Shah, K.; Robinson, J. A.; Chen, Z. Large-area, single-layer molybdenum disulfide synthesized at BEOL compatible temperature as Cu diffusion barrier. IEEE Electron Device Letters **2018**, *39*, 873–876.

(37) Smithe, K. K.; Zhu, Z.; Bailey, C. S.; Pop, E.; Yoon, A. In 2018 IEEE International Reliability Physics Symposium (IRPS), 2018, P–PI.

(38) Deijkers, J. S. H.; de Jong, A. A.; Mattinen, M. J.; Schulpen, J. J.; Verheijen, M. A.; Sprey, H.; Maes, J. W.; Kessels, W. E. M.; Bol, A. A.; Mackus, A. J. MoS2 Synthesized by Atomic Layer Deposition as Cu Diffusion Barrier. Advanced Materials Interfaces **2023**, *10*, 2202426.

(39) Nies, C. L.; Nolan, M. DFT calculations of the structure and stability of copper clusters on MoS2. Beilstein Journal of Nanotechnology **2020**, *11*, 391–406.

(40) Sweetman, M.; Nies, C.-L.; Nolan, M. Structure and stability of copper nanoclusters on monolayer tungsten dichalcogenides. Dalton Transactions **2025**, *54*, 3833–3846.

(41) Pedreira, O. V.; Croes, K.; Leśniewska, A.; Wu, C.; van der Veen, M. H.; de Messemaeker, J.; Vandersmissen, K.; Jourdan, N.; Wen, L.; Adelmann, C.; Briggs, B.; Gonzalez, V. V.; Bömmels, J.; Tőkei, Z. In 2017 IEEE International Reliability Physics Symposium (IRPS), 2017, 6B–2.

(42) Bekiaris, N.; Wu, Z.; Ren, H.; Naik, M.; Park, J. H.; Lee, M.; Ha, T. H.; Hou, W.; Bakke, J. R.; Gage, M.; Wang, Y.; Tang, J. In 2017 IEEE International Interconnect Technology Conference (IITC), 2017, pp 1–3.

(43) Gall, D. The search for the most conductive metal for narrow interconnect lines. Journal of Applied Physics **2020**, *127*, 050901.

(44) Pedreira, O. V.; Stucchi, M.; Gupta, A.; Gonzalez, V. V.; van der Veen, M.; Lariviere, S.; Wilson, C.; Tőkei, Z.; imec, K. C. In 2020 IEEE International Reliability Physics Symposium (IRPS), 2020, pp 1–7.

(45) Philip, T. M.; Lanzillo, N. A.; Gunst, T.; Markussen, T.; Cobb, J.; Aboud, S.; Robison, R. R. First-Principles Evaluation of fcc Ruthenium for its use in Advanced Interconnects. Physical Review Applied **2020**, *13*, 044045.

(46) Xie, L.-Y.; Zhang, J.-M. Electronic structures and magnetic properties of the transition-metal atoms (Mn, Fe, Co and Ni) doped WS2: a first-principles study. Superlattices and Microstructures **2016**, *98*, 148–157.

(47) Poornimadevi, C.; Kala, C. P.; Thiruvadigal, D. J. Tuning the electronic properties of WS2 monolayer by doping transition metals: DFT Approach. Materials Science in Semiconductor Processing **2023**, *157*, 107339.

(48) Xu, W. Electronic Structures and Magnetic Properties of Co-Adsorbed Monolayer WS2. Journal of Materials Science and Chemical Engineering **2016**, *04*, 32–41.

(49) majd, Z. G.; Taghizadeh, S. F.; Amiri, P.; Vaseghi, B. Half-metallic properties of transition metals adsorbed on WS2 monolayer: A first-principles study. Journal of Magnetism and Magnetic Materials **2019**, *481*, 129–135.

(50) Thomas, J. C.; Chen, W.; Xiong, Y.; Barker, B. A.; Zhou, J.; Chen, W.; Rossi, A.; Kelly, N.; Yu, Z.; Zhou, D.; Kumari, S.; Barnard, E. S.; Robinson, J. A.; Terrones, M.; Schwartzberg, A.; Ogletree, D. F.; Rotenberg, E.; Noack, M. M.; Griffin, S.; Raja, A.; Strubbe, D. A.; Rignanese, G.-M.; Weber-Bargioni, A.; Hautier, G. A substitutional quantum defect in WS2 discovered by high-throughput computational screening and fabricated by site-selective STM manipulation. Nature communications **2024**, *15*, 3556.

(51) Zhang, H.; Zhou, W.; Jiang, J.; Zeng, W.; Zhou, Q. First-Principles Investigation of Transition Metal (Co, Rh, and Ir)-Modified WS2 Monolayer Membranes: Adsorption and Detection of SF6 Decomposition Gases. ACS Applied Nano Materials **2024**, *7*, 13379–13391.

(52) Cao, L.; Ma, R.; Ran, M.; Cui, H. First-principles investigation on Ru-doped janus WSSe monolayer for adsorption of dissolved gases in transformer oil: A novel sensing candidate exploration. Sensors **2024**, *24*, 5967.

(53) Kim, J.-H.; Sakaguchi, I.; Hishita, S.; Ohsawa, T.; Suzuki, T. T.; Saito, N. Ru-implanted WS2 nanosheet gas sensors to enhance sensing performance towards CO gas in self-heating mode. Sensors and Actuators B: Chemical **2022**, *370*, 132454.

(54) Natarajan, S. K.; Nies, C. L.; Nolan, M. The role of Ru passivation and doping on the barrier and seed layer properties of Ru-modified TaN for copper interconnects. Journal of Chemical Physics **2020**, *152*, 144701.

(55) Nies, C.-L.; Natarajan, S. K.; Nolan, M. Control of the Cu morphology on Ru-passivated and Ru-doped TaN surfaces–promoting growth of 2D conducting copper for CMOS interconnects. Chemical Science **2022**, *13*, 713–725.

(56) Nies, C.-L.; Nolan, M. Incorporation of tungsten or cobalt into TaN barrier layers controls morphology of deposited copper. Journal of Physics: Materials **2023**, *6*, 035008.

(57) Nies, C. L.; Nolan, M. Prediction of Co and Ru nanocluster morphology on 2D MoS2 from interaction energies. Beilstein Journal of Nanotechnology **2021**, *12*, 704–724.

(58) Champion, J. A. Some properties of (Mo, W) (Se, Te)2. British Journal of Applied Physics **1965**, *16*, 1035.

(59) Brown, B. E. The crystal structures of WTe 2 and high-temperature MoTe 2. Acta Crystallographica **1966**, *20*, 268–274.

(60) Dawson, W. G.; Bullett, D. W. Electronic structure and crystallography of MoTe2and WTe2. Journal of Physics C: Solid State Physics **1987**, *20*, 6159.

(61) Li, S.; Lei, F.-c.; Peng, X.; Wang, R.-q.; Xie, J.-f.; Wu, Y.-p.; Li, D.-s. Synthesis of semiconducting 2H-phase WTe2 nanosheets with large positive magnetoresistance. Inorganic Chemistry **2020**, *59*, 11935–11939.

(62) Gong, C.; Zhang, H.; Wang, W.; Colombo, L.; Wallace, R. M.; Cho, K. Band alignment of two-dimensional transition metal dichalcogenides: Application in tunnel field effect transistors. Applied Physics Letters **2013**, *103*, 053513.

(63) Lee, C.-H.; Silva, E. C.; Calderin, L.; Nguyen, M. A. T.; Hollander, M. J.; Bersch, B.; Mallouk, T. E.; Robinson, J. A. Tungsten ditelluride: a layered semimetal. Scientific Reports **2015**, *5*, 10013.

(64) Kresse, G.; Furthmüller, J. Efficient iterative schemes for ab initio total-energy calculations using a plane-wave basis set. Physical Review B - Condensed Matter and Materials Physics **1996**, *54*, 11169–11186.

(65) Perdew, J. P.; Burke, K.; Ernzerhof, M. Generalized gradient approximation made simple. Physical Review Letters **1996**, *77*, 3865–3868.

(66) Blöchl, P. E. Projector augmented-wave method. Physical Review B **1994**, *50*, 17953–17979.

(67) Kresse, G.; Joubert, D. From ultrasoft pseudopotentials to the projector augmented-wave method. Physical Review B **1999**, *59*, 1758.

(68) Henkelman, G.; Jónsson, H. Improved tangent estimate in the nudged elastic band method for finding minimum energy paths and saddle points. The Journal of chemical physics **2000**, *113*, 9978–9985.

(69) Henkelman, G.; Uberuaga, B. P.; Jónsson, H. A climbing image nudged elastic band method for finding saddle points and minimum energy paths. The Journal of chemical physics **2000**, *113*, 9901–9904.

(70) Larsen, A. H.; Mortensen, J. J.; Blomqvist, J.; Castelli, I. E.; Christensen, R.; Dułak, M.; Friis, J.; Groves, M. N.; Hammer, B.; Hargus, C.; Hermes, E. D.; Jennings, P. C.; Jensen, P. B.; Kermode, J.; Kitchin, J. R.; Kolsbjerg, E. L.; Kubal, J.; Kaasbjerg, K.; Lysgaard, S.; Maronsson, J. B.; Maxson, T.; Olsen, T.; Pastewka, L.; Peterson, A.; Rostgaard, C.; Schiøtz, J.; Schütt, O.; Strange, M.; Thygesen, K. S.; Vegge, T.; Vilhelmsen, L.; Walter, M.; Zeng, Z.; Jacobsen, K. W. The atomic simulation environment - A Python library for working with atoms. Journal of Physics Condensed Matter **2017**, *29*, 273002.

(71) Momma, K.; Izumi, F. VESTA 3 for three-dimensional visualization of crystal, volumetric and morphology data. Journal of Applied Crystallography **2011**, *44*, 1272–1276.

(72) Henkelman, G.; Arnaldsson, A.; Jónsson, H. A fast and robust algorithm for Bader decomposition of charge density. Computational Materials Science **2006**, *36*, 354–360.

(73) Sanville, E.; Kenny, S. D.; Smith, R.; Henkelman, G. Improved grid-based algorithm for Bader charge allocation. Journal of computational chemistry **2007**, *28*, 899–908.

(74) Clementi, E.; Raimondi, D.-L. Atomic screening constants from SCF functions. The Journal of Chemical Physics **1963**, *38*, 2686–2689.

(75) Clementi, E.; Raimondi, D.; Reinhardt, W. P. Atomic screening constants from SCF functions. II. Atoms with 37 to 86 electrons. The Journal of chemical physics **1967**, *47*, 1300–1307.

(76) Huang, Y.-S.; Chen, Y.-F. Electronic-structure study of RuS 2. Physical Review B **1988**, *38*, 7997.